The Controllable Three-Dimensional Printing of Graphene/Nano-Hydroxyapatite Composite Scaffolds

Ao Shi*, Ting Huang

School of Materials and Chemistry, University of Shanghai for Science and Technology,
Shanghai 200093, China

*Corresponding author Email: 1967618730@qq.com

Abstract

Three-dimensional (3D) printing technology has garnered widespread attention in materials design and manufacturing due to its advantages of convenience, precision, speed, strong controllability, and ability to design and fabricate complex structures. In-depth research and development of 3D printing for various functional materials have significant implications. In this study, a gas-extrusion-based 3D printer was used to successfully fabricate graphene/hydroxyapatite (HA) composite scaffolds, exploring their potential applications in bone tissue engineering and lithium batteries. Graphene oxide (GO) aqueous solution was prepared using the Hummers method, followed by concentration and mixing with sodium alginate (SA) to form graphene hydrogel. Subsequently, different amounts of HA nanoparticles were added to fabricate HA/GO-SA and GO-SA composite scaffolds using gas-extrusion-based 3D printing. The scaffolds exhibited a well-ordered, interconnected macroporous structure, with HA/GO-SA scaffold pore diameters of approximately 300 μm and GO-SA scaffold pore diameters of approximately 500 μm, confirming the printability of graphene hydrogel. The compressive strength of the scaffolds was generally low, but the GO-SA scaffolds demonstrated certain elasticity. GO and GO-SA scaffolds were reduced using thermal and chemical reduction methods, and after HI reduction, the mechanical strength of the scaffolds was improved. Four-probe testing results confirmed that the conductivity of the reduced scaffolds was significantly enhanced.

Keywords

Gas-extruded 3D Printing; Bone Regenerating Scaffolds; Graphene; Micro Electrodes.

1. Introduction

In recent years, extensive research has been conducted on substituting mineral ions within the hydroxyapatite (HA) structure to enhance its biocompatibility [1-4]. By doping HA with various elements such as Mg, Sr, Zn, Ce, and La, the cellular activities during tissue regeneration can be regulated, as these elements play crucial roles in bone metabolism. However, due to the inherent brittleness of HA, its mechanical properties do not meet the requirements for osteogenesis, limiting its clinical applications. To improve the mechanical properties of HA, it can be composited with bioactive ceramics such as synthetic carbon nanofibers (CNFs), carbon nanotubes (CNTs), or graphene and its derivatives [5, 6]. Compared to CNTs, graphene and its derivatives are easier to synthesize with higher purity and exhibit lower cytotoxicity [7-9].

Graphene is a two-dimensional (2D) crystal composed of a single layer of carbon atoms, where each carbon atom undergoes sp^2 hybridization, forming a tightly packed honeycomb structure. Graphene oxide (GO) is a derivative of graphene. Compared to graphene, GO contains various oxygen-containing functional groups such as hydroxyl, epoxy, carboxyl, and carbonyl groups [10], with most carbon atoms forming sp^3 hybridized bonds with oxygen. The presence of oxygen-containing groups improves GO's dispersibility in aqueous solutions and provides anchoring sites for proteins, biomacromolecules, and inorganic nanoparticles. Additionally, GO possesses a large specific surface area, good biocompatibility, and excellent electrical properties. Previous studies have demonstrated that GO can selectively promote the osteogenic differentiation of stem cells, and its electrical conductivity can be utilized for electrical stimulation to induce osteogenesis. Moreover, GO facilitates HA deposition in simulated body fluid (SBF) [11]. Therefore, graphene and its derivatives hold significant potential in biomedical applications, including biosensing, drug delivery, and bioimaging.

Currently, biomaterials enhanced with graphene or graphene derivatives include hydroxyapatite (HA), chitosan, and hyaluronic acid, among others. The resulting composite materials exhibit excellent mechanical properties, biocompatibility, and drug delivery capabilities. For example, Li et al. [12] designed a novel hyaluronic acid-conjugated graphene oxide (HA-GO) system, with a size of several tens of nanometers, as a nanocarrier for photodynamic therapy. This system integrates the cancer-targeting ability of hyaluronic acid with the switchable photoactivity of a photosensitizer. The HA-GO conjugate combines the biocompatibility and degradability of HA with the water dispersibility and stability of GO. Through specific interactions with HA receptors on the cell surface, the HA-GO conjugate selectively targets HeLa cells, enabling the direct delivery of the photosensitizer chlorin e6 (Ce6) to cancer cells. This composite approach holds great potential for the targeted intracellular delivery of other hydrophobic drugs with aromatic structures, thereby enhancing therapeutic efficiency. Zhang et al. [13] synthesized graphene/hydroxyapatite (HA) composites using spark plasma sintering (SPS). Raman spectroscopy confirmed the preservation of graphene nanosheets (GNSs) under the harsh SPS processing conditions. Compared to pure HA, the fracture toughness of the 1.0 wt.% GNS/HA composite was improved by 80%. In vitro osteoblast growth experiments demonstrated that the addition of GNSs enhanced osteoblast adhesion and apatite mineralization. Therefore, graphene-hydroxyapatite composites hold great promise as ideal materials for load-bearing orthopedic implants.

Graphene materials, owing to their exceptional physicochemical properties, have demonstrated significant potential in energy storage devices within the energy sector. However, studies have shown that two-dimensional graphene materials tend to aggregate and stack, reducing their surface energy and thereby limiting their practical applications. As a result, extensive research has been conducted on three-dimensional (3D) graphene structures. Marcus et al. [14] successfully synthesized ultra-low-density 3D graphene nanosheets using the sol-gel method, which exhibited high electrical conductivity and a large internal surface area. In laboratory experiments, a chemically cross-linked suspension of monolayer graphene oxide (GO) was subjected to supercritical drying and subsequently thermally reduced to obtain graphene aerogels. The resulting 3D graphene sheets had a density of approximately 10 mg/cm^3. Shi et al. [15] developed 3D graphene foams under laboratory conditions using near-infrared irradiation, forming a 3D network with hydrophobic properties and high absorption capacity for organic liquids. Other synthesis methods for 3D graphene structures include electrodeposition [16], vacuum filtration [17], and hydrothermal synthesis [18, 19]. However, the size, morphology, and ratio of 3D graphene structures remain somewhat random, making precise design challenging. 3D printing technology, with its advantages of rapid prototyping and personalized customization, presents a promising solution to this issue. In this study, graphene oxide (GO) aqueous solution was prepared using the Hummers method. The GO solution was combined with sodium alginate (SA) to form a GO hydrogel. Hydroxyapatite (HA) was then incorporated into the hydrogel to create a HA/GO-SA composite, which, along with GO-SA, was fabricated into a porous scaffold using 3D printing technology. The study explores the relationship between fabrication process parameters, material composition, and the properties of the composite scaffold. Additionally, the GO hydrogel was reduced to obtain reduced graphene. This research investigates the controllable preparation of 3D graphene hydrogel structures using 3D printing technology and examines the electrical conductivity of 3D graphene hydrogels before and after reduction.

2. Experimental Section

Experimental Reagents: Hydroxyapatite (HA, ≥97%, Sigma-Aldrich), graphite powder (≥99%, Sinopharm Chemical Reagent Co., Ltd.), sodium nitrate ($NaNO_3$, ≥99%, Sinopharm Chemical Reagent Co., Ltd.), concentrated sulfuric acid (H_2SO_4, 98%, Sinopharm Chemical Reagent Co., Ltd.), potassium permanganate ($KMnO_4$, 99.0–100.5%, Sinopharm Chemical Reagent Co., Ltd.), hydrogen peroxide (H_2O_2, ≥30%, Sinopharm Chemical Reagent Co., Ltd.), concentrated hydrochloric acid (HCl, ≥36%, Sinopharm Chemical Reagent Co., Ltd.), hydroiodic acid (HI, 55–57%, Adamas Reagent Co., Ltd.), sodium alginate (SA, Sigma-Aldrich).

The experiment adopted the Hummers method [20] to prepare graphene oxide (GO). The specific preparation process is as follows: 5 g of expanded graphite powder (EG), 2.5 g of $NaNO_3$, and 115 mL of concentrated H_2SO_4 were sequentially added to a clean 1 L beaker and stirred slowly until well mixed. The mixture was stirred in an ice-water bath (temperature maintained below 10°C) for 25 minutes. Then, 15 g of $KMnO_4$ was slowly added to the mixture (the addition must be slow), followed by stirring for another 25 minutes while gradually increasing the temperature. When the solution reached 35°C, it was maintained in a 35°C water bath and stirred for 45 minutes. Afterward, 230 mL of deionized water was added, and the temperature of the water bath was raised to 98°C, followed by continuous stirring for 45 minutes. During this process, the mixture gradually changed from brownish to a bright yellow color. Then, the solution was diluted to 700 mL with deionized water at approximately 60°C. Next, 30 mL of 30% H_2O_2 solution was added, and the mixture was stirred for 10 minutes before being removed and left to cool. All operations were conducted in a water bath. Once the solution cooled to room temperature, 20 mL of HCl solution was added and stirred thoroughly. The treated solution was centrifuged and washed repeatedly until the pH of the supernatant was approximately 7. The centrifuged solution was transferred into a sealable glass bottle and subjected to ultrasonic treatment for 2 hours, with water replacement every 20 minutes to maintain a low-temperature ultrasonic environment. The final GO solution was sealed and stored for further use.

To prepare a slurry suitable for 3D printing of composite scaffolds, raw materials were mixed in appropriate proportions. First, the previously prepared GO solution was evaporated and concentrated to a final concentration of 6.5 mg/mL. A specific volume of the concentrated GO solution was measured, and an appropriate amount of sodium alginate (SA) powder was added. The mixture was heated in a 90°C water bath and stirred thoroughly until fully dissolved. Continuous heating and concentration resulted in the formation of GO hydrogel.

Next, nano-hydroxyapatite (HA) powder, which had been sieved through a 400-mesh screen, was added to obtain three groups of slurries with GO:HA mass ratios of 10:1, 6:1, and 2:1. Additionally, two control groups of slurries without HA powder were prepared. To ensure a smooth and fine texture for printing, all five final slurry formulations were passed through a 400-mesh sieve before use. The HA/GO/SA composite scaffolds were fabricated using a gas-extrusion-based 3D printer (Fourth-generation 3D Bioplotter™, EnvisionTEC GmbH, Germany). The process was as follows: The prepared injectable slurry was transferred into a polymer syringe and securely mounted onto the 3D Bioplotter™ system. A scaffold model with dimensions of 10 × 10 × 5 mm was designed using Bioplotter CAD/CAM software, with layer numbers set to 5 and 15. The printing process involved extruding the slurry layer by layer to form scaffolds, with the injection pump's gas pressure and printing speed set according to the parameters listed in Table 3-1. A nozzle with a diameter of 0.4 mm was used.

The five scaffold groups were named HA/GO-SA-1, HA/GO-SA-2, HA/GO-SA-3, GO-SA-1, and GO-SA-2. Finally, all scaffolds underwent freeze-drying treatment before further analysis.

This study attempted two methods to reduce the GO-SA composite scaffolds: thermal reduction and chemical reduction. Thermal Reduction: The freeze-dried GO-SA composite scaffolds were placed in a ceramic crucible and sintered at 1000°C in an argon atmosphere. The sintering procedure was as follows: the tube furnace was first purged with argon gas for 30 minutes to remove residual air, then heated to 600°C over 2 hours, maintained at this temperature for 2 hours, and finally cooled naturally according to the programmed setting. Chemical Reduction: Using hydroiodic acid (HI) as the reducing agent, the freeze-dried GO-SA composite scaffolds were immersed in a beaker containing HI solution at a scaffold-to-HI mass ratio of 1:10. The beaker was then placed in a 100°C oil bath, where the mixture was stirred slowly for 1 hour. After the reaction, the scaffolds were removed, washed five times with deionized water, and freeze-dried.

The scanning electron microscopy (SEM) images of GO were obtained using an FEI Quanta 450 field emission scanning electron microscope. The structure and composition of the prepared GO were analyzed using an X-ray diffractometer (XRD) from Bruker, with Cu-Kα radiation ($\lambda = 0.154056$ nm), a 2θ scan range of 10°-90°, and a scan rate of 5°/min. The testing method involved a pelletizing approach, where the GO sample was spread evenly on a glass plate, pressed into a flat surface, and then placed in the XRD system for data acquisition to determine the sample's structural composition. The SEM images of the five scaffold groups were also obtained using the FEI Quanta 450 field emission scanning electron microscope. The mechanical strength of the scaffolds was tested using a Zwick static material testing machine with a 2.5 kN load capacity, at a test speed of 0.5 mm/min. The scaffold dimensions were 10 × 10 × 5 mm. Wide-angle XRD diffraction patterns of the scaffolds were acquired using a Bruker D8 Advance X-ray diffractometer. The electrical conductivity of GO and the GO-SA scaffolds before and after reduction was measured using a four-probe station. Scaffold dimensions were 10 × 10 × 2 mm, and multiple test points were selected. The input voltage range was controlled from -1V to 1V, and the current variation within this range was recorded. Multiple measurements were taken, and the average value was used to calculate the resistivity.

3. Result and Discussion

3.1 Characterization of the Morphology and Structure of GO

Figure 1 shows the SEM images of the prepared graphene oxide (GO). From the SEM images, it can be observed that the prepared GO exhibits a wrinkled, uneven sheet-like morphology with a certain thickness and some degree of flexibility. Generally, SEM images of monolayer graphene reveal an uneven surface with wrinkles. To reduce the surface energy of graphene, the morphology of monolayer graphene tends to transition from an uneven two-dimensional structure to a more planar three-dimensional structure. Consequently, monolayer graphene exhibits more pronounced surface wrinkles compared to bilayer or multilayer graphene, and as the number of layers increases, the degree of surface wrinkling gradually decreases. Additionally, the XRD pattern of GO (Figure 2(A)) shows a distinct diffraction peak at $2\theta = 10.66°$, corresponding to the (002) plane of oxidized graphite. This indicates an interlayer spacing of 0.829 nm, which is increased due to the presence of abundant oxygen-containing functional groups, such as hydroxyl, carboxyl, and epoxy groups, between the graphite layers. The characteristic Raman scattering peaks of graphitic carbon typically include the D peak near 1350 cm^{-1} and the G peak near 1580 cm^{-1}, which correspond to sp^3 and sp^2 hybridized carbon, respectively. A lower ID/IG ratio indicates a higher degree of graphitization. Figure 3-2(B) presents the Raman spectrum of the synthesized GO, showing the D and G peaks at 1344 cm^{-1} and 1593 cm^{-1}, respectively.

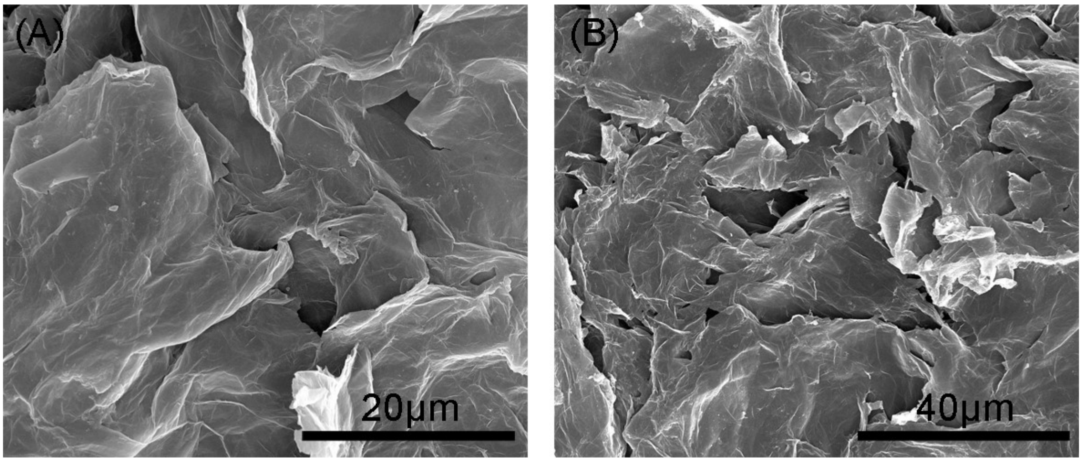

Figure 1. SEM images of GO

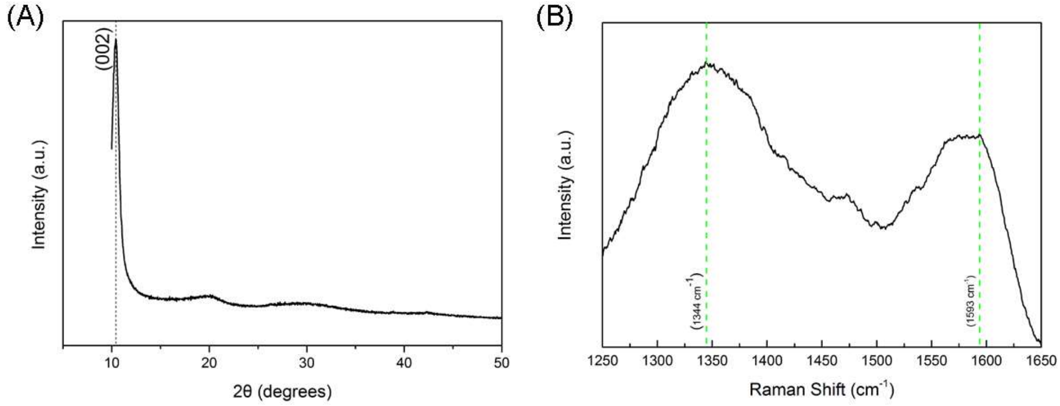

Figure 2. (A) XRD pattern of GO; (B) Raman spectrum of GOSEM images of GO

Figure 3 shows SEM images of HA/GO-SA-1, HA/GO-SA-2, HA/GO-SA-3, GO-SA-1, and GO-SA-2 scaffolds at different magnifications. As the GO content in the slurry increases, the printing pressure exhibits a decreasing trend, while the printing speed increases. This phenomenon is attributed to the rheological properties of graphene hydrogels, which possess good flowability. With a decrease in HA particle content, the resistance in the nozzle during printing decreases, leading to a reduction in printing pressure and an increase in printing speed. Additionally, the GO-SA-1 and GO-SA-2 scaffolds, which contain only GO and SA, demonstrate that graphene oxide hydrogel can be directly used for 3D printing. However, due to the relatively low viscosity of the graphene oxide aqueous solution, further exploration of printing parameters for high-ratio graphene oxide hydrogels is still needed. From the SEM images, it can be observed that using the 3D Bioplotter™, the HA/GO-SA and GO-SA scaffolds fabricated through layer-by-layer deposition exhibit a well-defined macroporous structure with interconnected pores. The pore diameter of HA/GO-SA (A1, B1, C1) scaffolds is approximately 300 μm, while that of GO-SA (D1, E1) scaffolds is around 500 μm. The layers are printed at a 90° angle relative to each other, and no structural collapse is observed between layers. The printed lines also maintain a good linear shape. As the HA particle content decreases, the HA/GO-SA scaffolds exhibit a rougher surface compared to GO-SA scaffolds. Since GO-SA scaffolds do not contain HA particles, their surfaces appear relatively smooth and flat, confirming the feasibility of fabricating 3D graphene oxide hydrogel scaffolds. The SEM images of GO-SA scaffolds (D1-E4) reveal a well-defined surface morphology, with tightly stacked GO layers. Compared to HA/GO-SA scaffolds, no significant cracks or fractures are observed on the surface. The scaffolds fabricated via 3D printing were subjected to freeze-drying treatment. During freeze-drying, the water content in the graphene hydrogel sublimates directly, leaving behind numerous pores. This process leads to the formation of cracks on the surface of HA/GO-SA scaffolds. As shown in Figure 3-1, GO exhibits a sheet-like structure. In the graphene hydrogel, graphene sheets are stacked layer by layer under the adhesive effect of SA. Due to the high surface energy of graphene sheets, they can maintain their structural integrity during freeze-drying, preserving the overall layered structure.

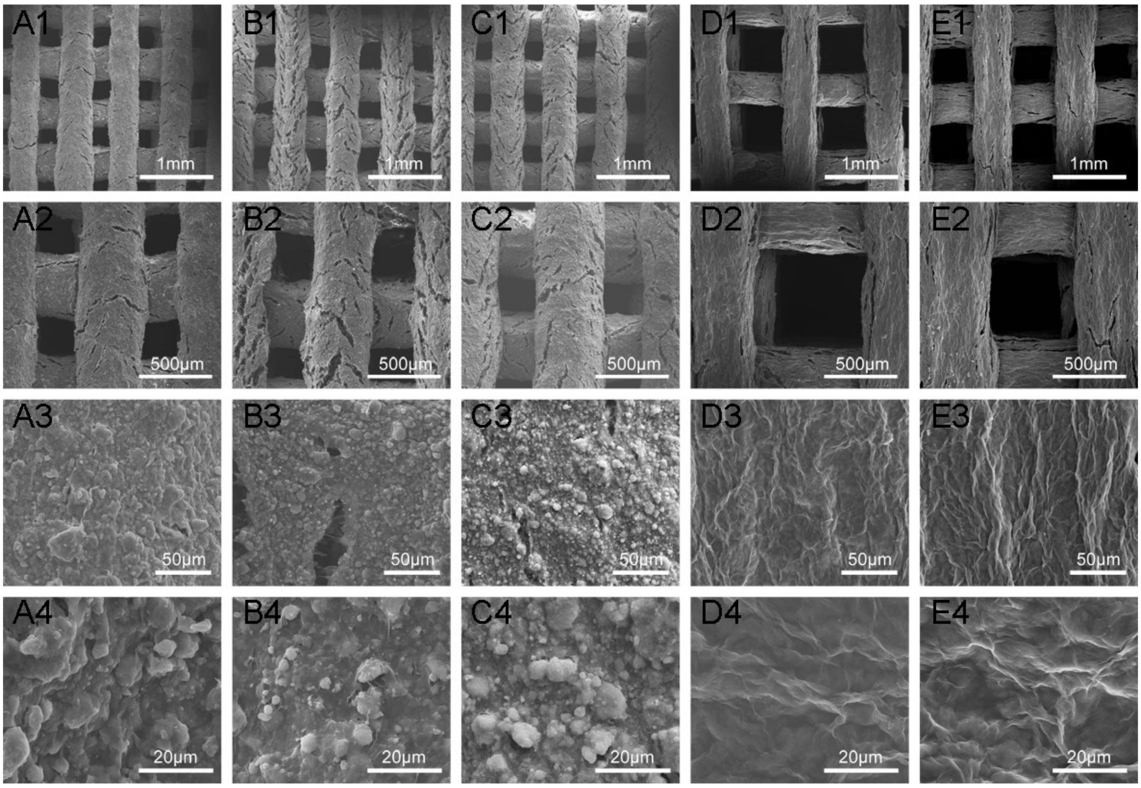

Figure 3. SEM images of scaffolds (A) HA/GO-SA-1, (B) HA/GO-SA-2, (C) HA/GO-SA-3, (D) GO-SA-1, and (E) GO-SA-2. (A1, B1, C1, D1, E1: 100×; A2, B2, C2, D2, E2: 200×; A3, B3, C3, D3, E3: 1500×; A4, B4, C4, D4, E4: 5000×) along with optical images of each scaffold.

Figure 4 shows the Raman spectra of HA/GO-SA scaffolds and GO-SA scaffolds. From the Raman spectra, it can be observed that the D and G peaks of graphene appear at approximately 1344 cm^{-1} and 1590 cm^{-1}, respectively, indicating that the presence and characteristics of GO were not significantly affected by the 3D printing process used to fabricate the HA/GO-SA and GO-SA scaffolds. As the amounts of HA and SA increased, the characteristic peaks of GO weakened to some extent but did not completely obscure its properties.

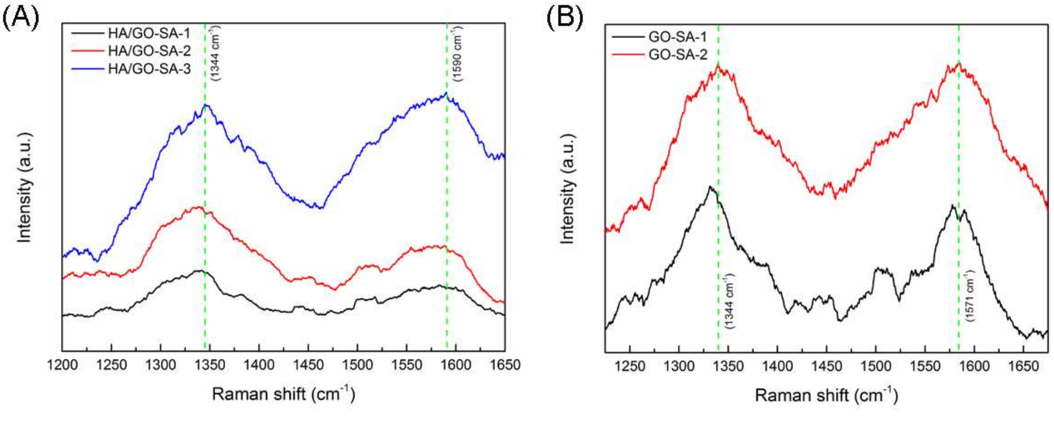

Figure 4. (A) Raman spectrum of HA/GO-SA scaffold; (B) Raman spectrum of GO-SA scaffold.

From the compression test results of the HA/GO-SA and GO-SA scaffolds (Figure 5(A)), the mechanical strengths of HA/GO-SA-1, HA/GO-SA-2, HA/GO-SA-3, GO-SA-1, and GO-SA-2 scaffolds were measured as 62 ± 2 Pa, 85 ± 3 Pa, 43 ± 1 Pa, 20 ± 1 Pa, and 17 ± 0.5 Pa, respectively. It can be observed that the compressive strength of HA/GO-SA scaffolds does not meet the requirements for human cancellous bone. This is attributed to the preparation method, where HA particles were incorporated into the graphene hydrogel and subsequently processed via 3D printing. Due to the high water content in the graphene hydrogel, the sublimation of water during freeze-drying resulted in a highly porous scaffold, which is consistent with the SEM images of HA/GO-SA scaffolds, thereby leading to their low compressive strength. Figure 5(B) presents the optical images of the scaffolds used for compression testing. #1 and #2 display the front and side views of the 3D-printed GO-SA scaffolds with dimensions of 10 × 10 × 5 mm. #3 shows the front view of the GO-SA scaffold after compression testing using a 2.5 kN Zwick static material testing machine, while #4 depicts a 3D-printed cylindrical GO-SA scaffold with a size of φ10 × 5 mm. A comparison of the optical images of the GO-SA scaffolds before and after compression testing (Figure 5(B)) indicates that the scaffolds did not undergo fracture or structural failure. Even when subjected to 80% strain, the scaffolds retained their 3D porous structure, demonstrating the presence of abundant internal porosity. Additionally, a series of simple resilience tests were conducted on the GO-SA scaffolds, as shown in Figure 6. When compressed by approximately 50%, the scaffold instantly recovered to around 70% of its original height, regained about 90% within 5 minutes, and fully recovered to its initial height within approximately 2 hours. Notably, the GO-SA-2 scaffold exhibited better resilience than the GO-SA-1 scaffold, indicating that a higher GO content enhances scaffold elasticity. However, when subjected to deformations exceeding 80%, the scaffold lost its ability to recover, as observed in #3 of Figure 5(B).

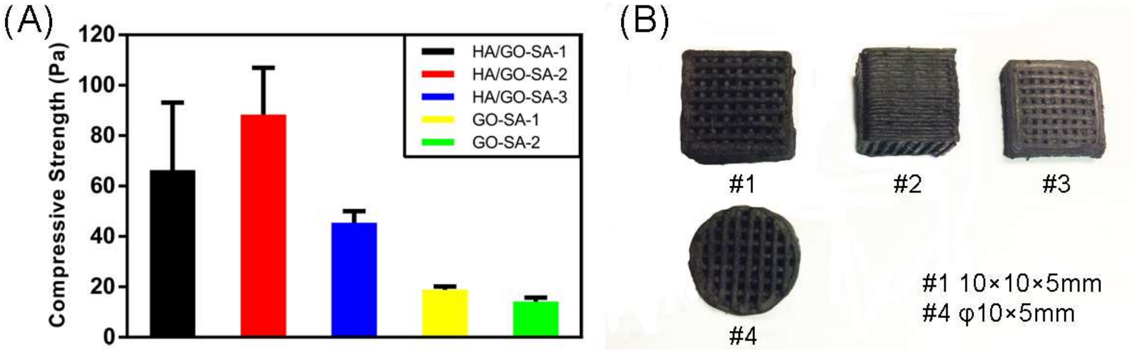

Figure 5. (A) Mechanical strength of HA/GO-SA and GO-SA scaffolds; (B) Optical images of GO-SA scaffolds before and after compression testing.

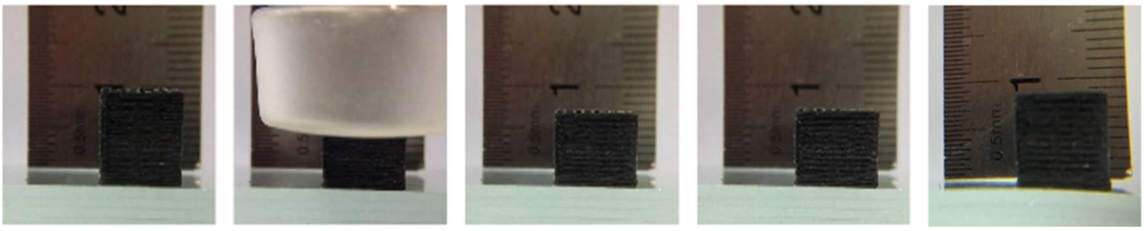

Figure 6. Elastic recovery test of GO-SA scaffolds.

The GO-containing composite scaffolds were subjected to high-temperature reduction and HI reduction. Due to the carbonization of the binder SA under high-temperature conditions and the absence of other solid-phase particles in the GO-SA scaffold, the thermally reduced GO-SA scaffold collapsed and failed to maintain its three-dimensional porous structure. Figure 7 presents SEM images of GO-SA-1 and GO-SA-2 scaffolds at different magnifications before and after HI acid reduction.

As observed in the images, the shrinkage rate of the GO-SA scaffold after HI reduction reached approximately 50%; however, the scaffold still retained its original three-dimensional structure after reduction. At a magnification of 5000×, it can be seen that after reduction, the graphene layers on the scaffold surface became more tightly packed, with increased wrinkling. Additionally, the mechanical strength of the chemically reduced GO-SA scaffold was improved. As the GO content increased, the changes in scaffold morphology and strength were relatively small, demonstrating the potential of higher GO-content graphene-based structures for three-dimensional printing applications.

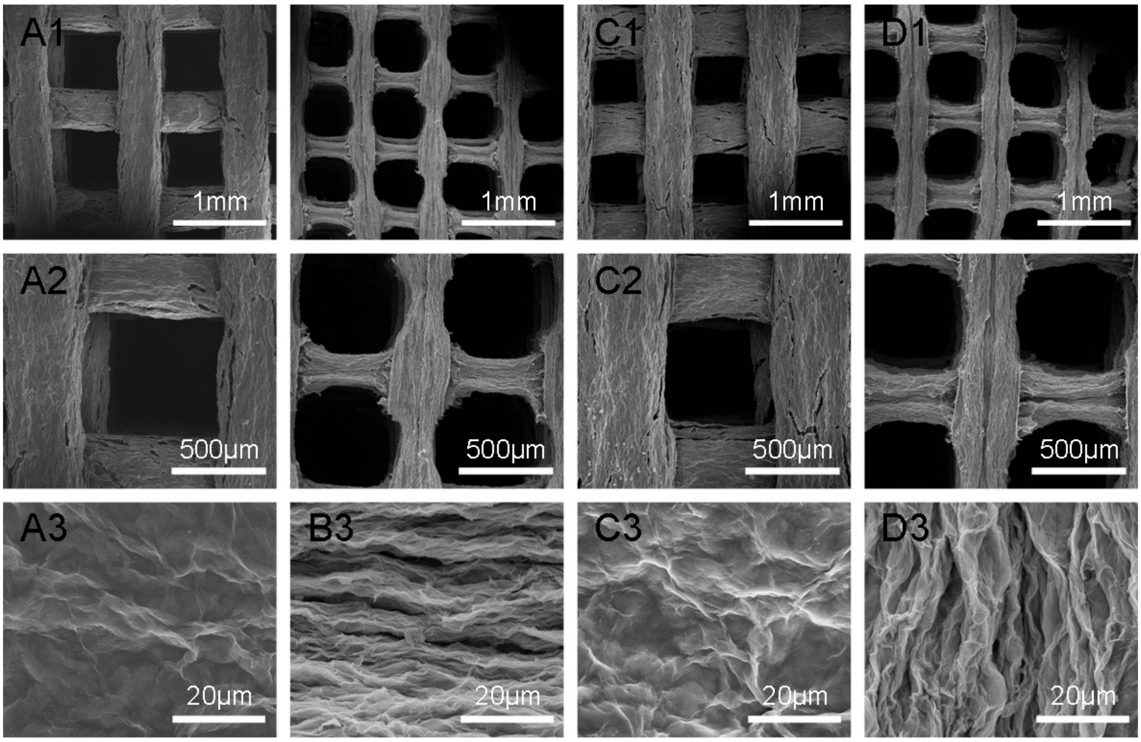

Figure 7. SEM images of GO-SA-1 and GO-SA-2 scaffolds before (A, C) and after (B, D) reduction. (A1, B1, C1, D1: 100×; A2, B2, C2, D2: 200×; A3, B3, C3, D3: 5000×).

3.2 Resistivity Testing of GO-SA Composite Scaffolds before and after Reduction

Figure 8 presents the electrical conductivity test results of GO and GO-SA composite scaffolds. The voltage range for testing was -1 to 1V. Based on the current measurements, the electrical conductivity of the unreduced GO-SA scaffold (Figure 8(A)) was calculated to be 2.9×10^{-7} S/m. In comparison, the electrical conductivity of the thermally reduced GO-SA scaffold (Figure 8(B)) was 2.9×10^{-3} S/m, showing a four-order magnitude increase after reduction. Additionally, the electrical conductivity of pure GO before and after thermal reduction was measured as 2.5×10^{-7} S/m (Figure 8(C)) and 8.6×10^{-3} S/m (Figure 8(D)), respectively. The four-order magnitude increase after reduction indicates that thermal reduction effectively restores graphene oxide. Furthermore, the presence of the binder SA in the scaffold did not significantly affect the electrical conductivity of the graphene material before or after thermal reduction. Figures 8(E) and 8(F) show the results of HI acid-reduced GO-SA-1 and GO-SA-2 scaffolds, with electrical conductivities of 2.5×10^{-2} S/m and 5.0×10^{-1} S/m, respectively. Compared to the electrical conductivity of the unreduced GO-SA scaffold, these values increased by five to six orders of magnitude, demonstrating that HI acid effectively reduces graphene oxide. The electrical conductivity of HI-reduced GO-SA-2 was higher than that of GO-SA-1, indicating that a higher graphene content results in better conductivity after reduction. However, despite washing, HI acid-reduced GO-SA scaffolds retained significant acidity, which may limit their applications. Therefore, both thermal reduction and HI acid reduction effectively restore graphene oxide and enhance the electrical conductivity of GO-SA scaffolds.

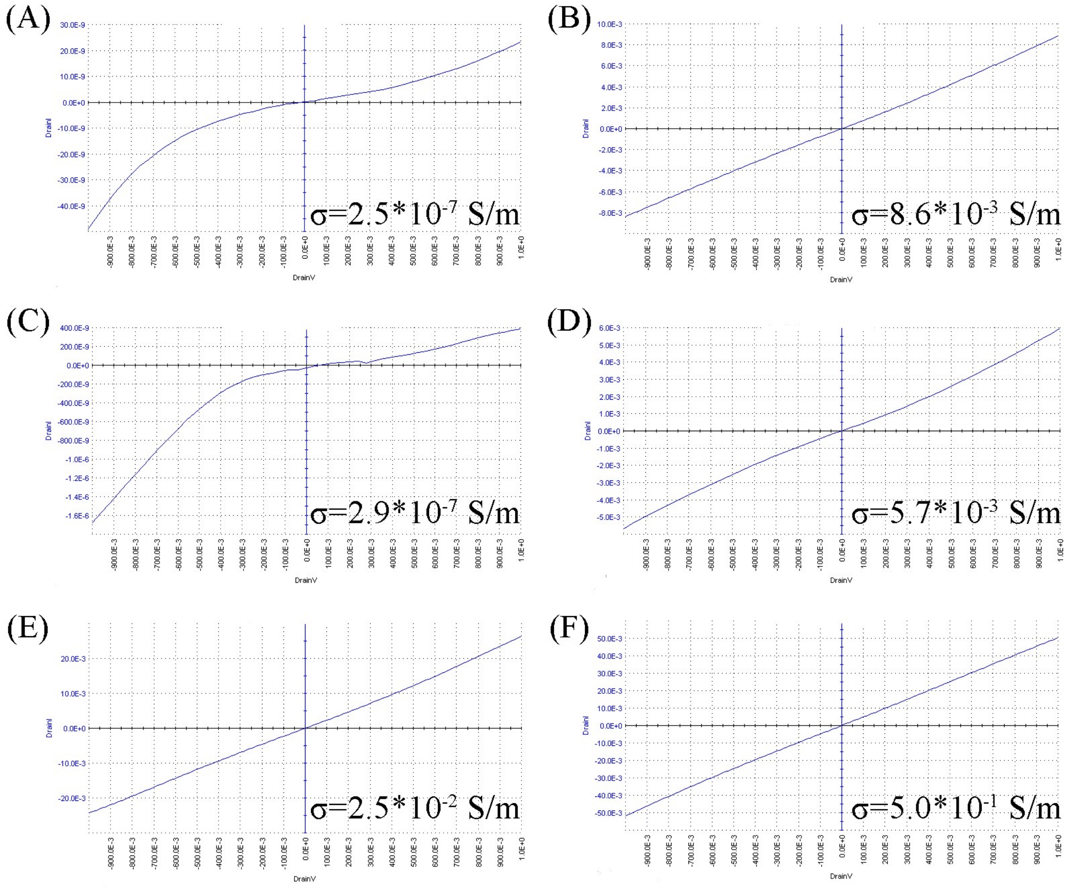

Figure 8. I-V Curves: (A) Unreduced GO; (B) Thermally reduced GO; (C) Unreduced GO-SA-1 scaffold; (D) Thermally reduced GO-SA-1 scaffold; (E) HI acid-reduced GO-SA-1 scaffold; (F) HI acid-reduced GO-SA-2 scaffold.

4. Conclusion

In this study, graphene oxide (GO) was successfully prepared using the Hummers method, with GO sheet sizes at the micron scale. Using sodium alginate (SA) as a binder, HA/GO-SA-1, HA/GO-SA-2, HA/GO-SA-3, GO-SA-1, and GO-SA-2 composite scaffolds were successfully fabricated via gas extrusion-based three-dimensional (3D) printing. The scaffolds exhibited a well-defined, interconnected macroporous structure, with pore diameters of approximately 300 μm for HA/GO-SA scaffolds and 500 μm for GO-SA scaffolds. As the HA particle content decreased, the surface roughness of the HA/GO-SA scaffolds also decreased, confirming the printability of graphene hydrogel. The compressive strength tests of HA/GO-SA scaffolds indicated poor mechanical properties, failing to meet the compressive strength requirements of human cancellous bone (2–12 MPa). Similarly, the mechanical strength of GO-SA scaffolds was relatively low. However, compression test results suggested that the scaffolds contained a large number of internal pores and exhibited a certain degree of resilience, warranting further exploration of potential applications. GO and GO-SA scaffolds were reduced using thermal and chemical reduction methods. The HI acid-reduced scaffolds retained their 3D structure, but residual acid was difficult to remove. In contrast, thermally reduced scaffolds exhibited poor mechanical strength and collapsed. However, four-probe electrical conductivity measurements showed a significant increase in the conductivity of the reduced scaffolds, indicating that reduced GO-SA scaffolds hold potential for electrical applications.

References

[1] Gopi D, Ramya S, Rajeswari D, et al. Strontium, cerium co-substituted hydroxyapatite nanoparticles: Synthesis, characterization, antibacterial activity towards prokaryotic strains and in vitro studies [J]. Colloids and Surfaces A: Physicochemical and Engineering Aspects, 2014, 451(172-80).

[2] Cox S C, Jamshidi P, Grover L M, et al. Preparation and characterisation of nanophase Sr, Mg, and Zn substituted hydroxyapatite by aqueous precipitation [J]. Mater Sci Eng C Mater Biol Appl, 2014, 35(106-14).

[3] Gopi D, karthika A, Nithiya S, et al. In vitro biological performance of minerals substituted hydroxyapatite coating by pulsed electrodeposition method [J]. Materials Chemistry and Physics, 2014, 144(1-2): 75-85.

[4] Moreira M P, De A S, Dentzer J, et al. Synthesis of magnesium- and manganese-doped hydroxyapatite structures assisted by the simultaneous incorporation of strontium [J]. Mater Sci Eng C Mater Biol Appl, 2016, 61(736-43).

[5] Zeng Y, Pei X, Yang S, et al. Graphene oxide/hydroxyapatite composite coatings fabricated by electrochemical deposition [J]. Surface & Coatings Technology, 2016, 286(72-9).

[6] Li M, Liu Q, Jia Z, et al. Graphene oxide/hydroxyapatite composite coatings fabricated by electrophoretic nanotechnology for biological applications [J]. Carbon, 2014, 67(185-97).

[7] Zeng Y, Pei X, Yang S, et al. Graphene oxide/hydroxyapatite composite coatings fabricated by electrochemical deposition [J]. Surface & Coatings Technology, 2016, 286(72-9).

[8] Li M, Liu Q, Jia Z, et al. Graphene oxide/hydroxyapatite composite coatings fabricated by electrophoretic nanotechnology for biological applications [J]. Carbon, 2014, 67(185-97).

[9] Jankovi´c A, Erakovi´c S, Vukaˇsinovi´c-sekuli´c M, et al. Graphene-based antibacterial composite coatings electrodeposited on titanium for biomedical applications [J]. Progress in Organic Coatings, 2015, 83(1-10).

[10] Krishnamoorthy K, Veerapandian M, YUN K, et al. The chemical and structural analysis of graphene oxide with different degrees of oxidation [J]. Carbon, 2013, 53(38-49).

[11] Gao F, Xu C, Hu H, et al. Biomimetic synthesis and characterization of hydroxyapatite/graphene oxide hybrid coating on Mg alloy with enhanced corrosion resistance [J]. Materials Letters, 2015, 138(25-8).

[12] Li F, Park S-J, Ling D, et al. Hyaluronic acid-conjugated graphene oxide/photosensitizer nanohybrids for cancer targeted photodynamic therapy [J]. Journal of Materials Chemistry B, 2013, 1(12): 1678.

[13] Zhang L, Liu W, Yue C, et al. A tough graphene nanosheet/hydroxyapatite composite with improved in vitro biocompatibility [J]. Carbon, 2013, 61(105-15).

[14] Worsley M, Pauzauskie P, Olson T, et al. Synthesis of Graphene Aerogel with High Electrical Conductivity [J]. Journal of the American Chemical Society, 2010, 132(14067-69).

[15] Shi Q, Hou C, Wang H, et al. Rapid formation of superelastic 3D reduced graphene oxide networks with simultaneous removal of HI utilizing NIR irradiation [J]. Journal of Materials Chemistry A, 2015, 3(18): 9882-9.

[16] He Y, Chen W, Li X, et al. Freestanding Three-Dimensional Graphene/MnO2 Composite Networks As Ultralight and Flexible Supercapacitor Electrodes [J]. Acs Nano, 2013, 7(174-82).

[17] Choi B, Yang M, Hong W, et al. 3D Macroporous Graphene Frameworks for Supercapacitors with High Energy and Power Densities [J]. Acs Nano, 2012, 6(4020-28.

[18] Zhao B, Huang S-Y, Wang T, et al. Hollow SnO2@Co3O4 core–shell spheres encapsulated in three-dimensional graphene foams for high performance supercapacitors and lithium-ion batteries [J]. Journal of Power Sources, 2015, 298(83-91).

[19] Burress J W, Gadipelli S, Ford J, et al. Graphene oxide framework materials: theoretical predictions and experimental results [J]. Angew Chem Int Ed Engl, 2010, 49(47): 8902-4.

[20] Dreyer D R, Park S, Bielawski C W, et al. The chemistry of graphene oxide [J]. Chem Soc Rev, 2010, 39(1): 228-40.